



HAL
open science

Nonlinear Force-Free Extrapolation of Emerging Flux with a Global Twist and Serpentine Fine Structures

G. Valori, L. Green, P. Demoulin, S. Vargas Domínguez, L. van Driel-Gesztelyi, A. Wallace, D. Baker, M. Fuhrmann

► **To cite this version:**

G. Valori, L. Green, P. Demoulin, S. Vargas Domínguez, L. van Driel-Gesztelyi, et al.. Nonlinear Force-Free Extrapolation of Emerging Flux with a Global Twist and Serpentine Fine Structures. *Solar Physics*, 2012, 278 (1), pp.73-97. 10.1007/s11207-011-9865-8. hal-02860257

HAL Id: hal-02860257

<https://hal.science/hal-02860257>

Submitted on 13 Jul 2022

HAL is a multi-disciplinary open access archive for the deposit and dissemination of scientific research documents, whether they are published or not. The documents may come from teaching and research institutions in France or abroad, or from public or private research centers.

L'archive ouverte pluridisciplinaire **HAL**, est destinée au dépôt et à la diffusion de documents scientifiques de niveau recherche, publiés ou non, émanant des établissements d'enseignement et de recherche français ou étrangers, des laboratoires publics ou privés.

Nonlinear Force-Free Extrapolation of Emerging Flux with a Global Twist and Serpentine Fine Structures

G. Valori · L.M. Green · P. Démoulin · S. Vargas Domínguez · L. van Driel-Gesztelyi · A. Wallace · D. Baker · M. Fuhrmann

Received: 11 February 2011 / Accepted: 6 September 2011 / Published online: 8 November 2011
© Springer Science+Business Media B.V. 2011

Abstract We study the flux emergence process in NOAA active region 11024, between 29 June and 7 July 2009, by means of multi-wavelength observations and nonlinear force-free extrapolation. The main aim is to extend previous investigations by combining, as much as possible, high spatial resolution observations to test our present understanding of small-scale (undulatory) flux emergence, whilst putting these small-scale events in the context of the global evolution of the active region. The combination of these techniques allows us to follow the whole process, from the first appearance of the bipolar axial field on the east limb, until the buoyancy instability could set in and raise the main body of the twisted flux tube through the photosphere, forming magnetic tongues and signatures of serpentine field, until the simplification of the magnetic structure into a main bipole by the time the active region reaches the west limb. At the crucial time of the main emergence phase high spatial resolution spectropolarimetric measurements of the photospheric field are employed to

Flux Emergence in the Hinode Era
Guest Editor: L.M. Green

G. Valori (✉) · P. Démoulin · L. van Driel-Gesztelyi
LESIA-Observatoire de Paris, CNRS, UPMC Univ. Paris 06, Univ. Paris-Diderot,
92195 Meudon Cedex, France
e-mail: gherardo.valori@obspm.fr

G. Valori
Institute of Physics and Astronomy, University of Potsdam, Karl-Liebknecht-Str. 24-25,
14476 Potsdam, Germany

L.M. Green · S. Vargas Domínguez · L. van Driel-Gesztelyi · A. Wallace · D. Baker
UCL-Mullard Space Science Laboratory, Holmbury St Mary, Dorking, Surrey RH5 6NT, UK

L. van Driel-Gesztelyi
Konkoly Observatory of the Hungarian Academy of Sciences, Budapest, Hungary

S. Vargas Domínguez
Departamento de Física, Universidad de Los Andes, AA.4976 Bogotá, Colombia

M. Fuhrmann
DYCOS, Universität Potsdam, Karl-Liebknecht-Str. 24/25, 14476 Potsdam, Germany

reconstruct the three-dimensional structure of the nonlinear force-free coronal field, which is then used to test the current understanding of flux emergence processes. In particular, knowledge of the coronal connectivity confirms the identity of the magnetic tongues as seen in their photospheric signatures, and it exemplifies how the twisted flux, which is emerging on small scales in the form of a sea-serpent, is subsequently rearranged by reconnection into the large-scale field of the active region. In this way, the multi-wavelength observations combined with a nonlinear force-free extrapolation provide a coherent picture of the emergence process of small-scale magnetic bipoles, which subsequently reconnect to form a large-scale structure in the corona.

Keywords Active regions, magnetic fields · Magnetic field, photosphere, corona

1. Introduction

Flux emergence into the solar atmosphere occurs on varying size scales, with the largest events forming active regions (hereafter ARs) with a flux range of 5×10^{21} to 4×10^{22} Mx (maxwell) (Schrijver and Harvey, 1994). The emerging flux carries with it the signatures of the dynamo process where the flux was created, of the convection zone through which it travelled, and of the conditions immediately below the photosphere where the flux accumulated and fragmented before emergence into the atmosphere became possible.

Initial descriptions of the flux emergence process involved the rise of a coherent Ω -shaped flux tube from the base of the convection zone, through the photosphere and into the corona (Zwaan, 1985). Observations have shown that emerging flux carries currents, which indicates that the flux must be twisted (Leka *et al.*, 1996). Indeed, a flux tube travelling through the convective zone must be twisted to some degree to prevent it being torn apart by vortices that develop in its wake (Schüssler, 1979; Longcope, Fisher, and Arendt, 1996; Moreno-Insertis and Emonet, 1996). Therefore, the rise of a coherent and monolithic twisted flux tube from the convection zone up to the lower photospheric layers was described as the buoyant emergence of a flux rope. Though a twisted emerging flux tube is a three-dimensional structure, the presence of magnetic twist can be recognised in longitudinal magnetograms due to the contribution of the azimuthal component. The twist is characterised by the presence of elongated polarities, called “magnetic tongues”. These patterns reflect the global twist of the flux rope as its apex crosses the photosphere (López Fuentes *et al.*, 2000; Luoni *et al.*, 2011), and reveal the sign of the twist (*i.e.*, whether it is left- or right-handed, negative or positive, respectively). The magnetic tongue patterns have also been successfully reproduced in magneto-hydrodynamics (MHD) simulations of twisted flux emergence (Archontis and Hood, 2010).

The current understanding of the structure of the emerging field is a slight modification of the above, based on observations of fine structure in the emerging regions, which suggest the presence of undulating “serpentine” field whilst the flux rope is breaking through the photosphere. Observationally, the serpentine field is seen as many small bipolar fragments in between the main, diverging, polarities (Strous and Zwaan, 1999; Bernasconi *et al.*, 2002). Physically, the serpentine field is related to the difficulties that the flux has in crossing the photospheric region. The rise of the flux rope slows and its upper part flattens as it approaches the photosphere. This is due to a rapid outward decrease in plasma pressure in the atmosphere, on a scale-height smaller than the flux rope cross-section size, so that the top part of the flux rope would become much denser than the surrounding atmosphere if it would continue to rise. As a result of the gravitational force there

is a pile-up of flux under the photosphere and a deformation of the upper part of the flux rope resulting in a serpentine shape (Pariat *et al.*, 2004). In order for the serpentine flux to emerge, reconnection must take place to remove the U-loop sections of the field which trap dense plasma and act to inhibit the emergence. The role of the sea-serpent in the emergence process was described using the linear force-free approximation (Schmieder *et al.*, 2000; Pariat *et al.*, 2004) and data-driven numerical simulations (Pariat, Masson, and Aulanier, 2009).

Once the serpentine field lines have emerged, they interact with the pre-existing, larger-scale flux system of the AR (Harra *et al.*, 2010). In this way, the emerging flux is thought to be merged by reconnection into the ambient coronal field.

The fragmentation and small-scale emergence processes that take place at the photosphere implies that the flux rope, which crossed the convective zone, is not emerging as one entity. Modern numerical simulations show that the flux rope axis is unable to emerge into the upper layers unless it is initially bent upward. Otherwise, the flux rope is destroyed and re-formed above the photosphere by reconnection (see the review of Hood, Archontis, and MacTaggart, 2011 and references therein). In the following we focus on the parts of the flux rope that have emerged.

In this paper we test the above picture of emergence for the NOAA AR 11024 by combining multi-wavelength observations and a nonlinear force-free field (NLFFF) extrapolation. The favourable position of this region on the disk and the excellent observational coverage allow us to follow the magnetic field evolution from the initial emergence of the AR, through the appearance of serpentine field lines, until their conversion from short field lines to large-scale coronal field. Similarly to other works, we study these processes using their photospheric and coronal signatures. However, we then proceed to verify that the three-dimensional coronal magnetic field, computed by NLFFF extrapolation, is indeed compatible with the current interpretation of such signatures. We perform the comparison at all scales, from AR-wide, through the intermediate scales of the magnetic tongues, down to the scale at which the serpentine field lines emerge. In this way we are able to attain a synthesis between observations on the one hand, and the associated coronal field topology on the other, which covers within a single frame all the relevant scales involved in the emergence and formation of the AR. Complementary studies of this AR discussed the emergence process of elementary flux tubes at the granular scale (Vargas Domínguez, van Driel-Gesztelyi, and Bellot Rubio, 2010), and the formation of the sunspot and its penumbra (Schlichenmaier *et al.*, 2010).

The paper is organised as follows: in Section 2 the data and their preparation details are given; in Section 3 the nonlinear magneto-frictional extrapolation method is briefly summarised; in Section 4 the observed evolution of the AR is discussed; in Section 5 the global quantities of the extrapolated field are analysed, whilst in Section 6 we combine the observations with the magnetic extrapolation to study the emergence processes; and finally, in Section 7, our conclusions are presented.

2. Instrumentation and Data Handling

The evolution of the magnetic field is studied using data of SOHO/MDI (Scherrer *et al.*, 1995), which measures the line-of-sight (LOS) magnetic field in the mid-photosphere, and data of the *Hinode*/SOT spectropolarimeter (Tsuneta *et al.*, 2008, hereafter SOT/SP), which measures the full Stokes profiles in the photosphere. The SOHO/MDI data are also used to determine the time evolution of flux in the region. For this purpose, the data are corrected

for the area foreshortening that occurs away from central meridian, and the radial field component is estimated using the IDL Solar Software routine `zradialise`.

To study the horizontal flows of photospheric magnetic features we employ local correlation tracking techniques (November and Simon, 1988, hereafter LCT). By using a Gaussian tracking window of full width at half maximum (FWHM) appropriate to the scale being examined ($1''$ or $3''$), we compute the proper motions of magnetic elements over the *Hinode*/Narrow Filter Imager (hereafter SOT/NFI) sequence of magnetograms. The time series used for this analysis starts at 12:00 UT on 4 July 2009 and is composed by 28 images with a cadence of 2 min.¹ Prior to applying LCT the sequence of images is aligned to eliminate possible jittering and rotation of the observing target within the field of view (hereafter FOV). Taking the first image as reference, the following images were aligned to it by correlating pairs of subsequent images and accumulating their apparent motions. A correlation window framing the entire AR was employed for this process. Images were finally trimmed to include only the area of the FOV that was present in all frames.

The corona is observed using the *Hinode*/EUV Imaging Spectrometer (hereafter EIS, Culhane *et al.*, 2007). EIS rasters from west to east and captures both spatial and spectral information simultaneously across multiple wavelengths. Images are processed using the IDL Solar Software routine `eis_prep` to perform dark current subtraction, removal of cosmic rays, hot, warm, saturated and dusty pixels and unit conversion to intensity per second. To extract the velocities in the slit data the spectrum was fitted with a Gaussian profile, and the Doppler velocity relative to a patch of quiet Sun was calculated for each pixel. Besides rastering, the $40''$ slot mode was used to obtain images in several emission lines for the entire AR. In the slot images, due to line blending, spectral velocities are not readily available. All EIS images are co-aligned with respect to the SOHO/MDI data.

Similarly, *Hinode*/X-Ray Telescope (hereafter XRT, Golub *et al.*, 2007) data obtained with the Ti-poly filter were preprocessed using the `xrt_prep` routine of IDL Solar Software, and co-aligned to the *Hinode*/SOT magnetogram data. The Ti-poly filter images plasma between 2 to 5 MK.

For the extrapolation we employed the vector magnetogram (provided by the *Hinode* team as level 2 data) obtained by inverting the spectropolarimetric measurements taken with SOT/SP on 4 July 2009, between 11:58 UT and 12:34 UT. The grid of level 2 data is composed of 312×384 nodes with constant resolution equal to $0.30''$ and $0.32''$, in x and y , respectively. The ambiguity in the orientation of the transverse component was removed using a recent implementation (Leka *et al.*, 2009) of the Minimum Energy method (see *e.g.*, Metcalf *et al.* (2006) and reference therein). Since the region is relatively far from Sun centre, strong projection effects, resulting in mixing of vertical and horizontal field components into the LOS and transverse components, occur. In order to reduce projection effects, the measured field was transformed into heliographic projection prior to extrapolation, following the method by Gary and Hagyard (1990). This transformation stretches, mostly in the y direction, the grid on which the level 2 data are provided. The vector field is then re-sampled onto a uniform, Cartesian grid of 293×424 of resolution $0.32''$ in both directions, on a plane that is tangent to the Sun at the central pixel of the SOT/SP FOV, located at $(-107'', -488'')$ in heliocentric coordinates.

Nonlinear force-free extrapolation of vector magnetograms may lead to ill-defined magnetic fields with an energy that is smaller than the energy of the potential field having the

¹The corresponding movie is provided as attached electronic material.

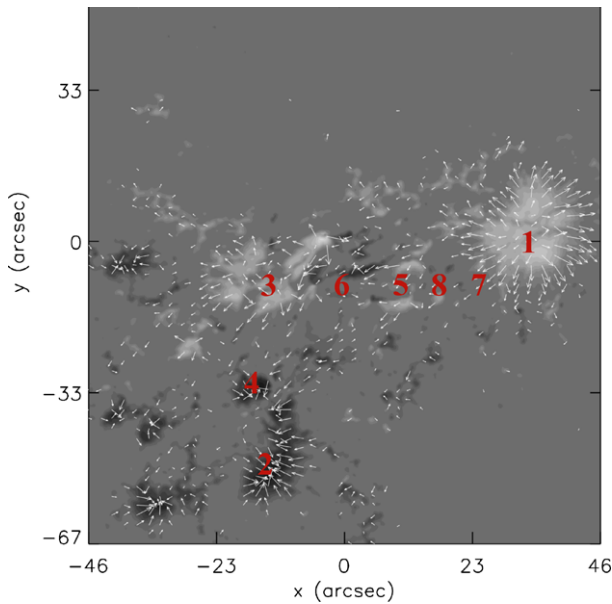


Figure 1 Vector magnetogram used as the boundary condition for the extrapolation, in the heliographic plane. The vertical field, ranging from -2409 G to 2965 G, is given in grey scale and the transverse component is indicated by arrows, with the longest arrow corresponding to 1818 G. Only values of the transverse field above 100 G are depicted. The main polarities involved in the analysis are numbered. (Even and odd numbers are used for positive and negative polarities, respectively. The polarity pairs are associated both by the photospheric field evolution and by the magnetic field extrapolation in Section 6, and they have consecutive numbers.) The photospheric field is derived from the SOT/SP scan on 4 July 2009 from 11:58 UT until 12:34 UT. The heliographic plane is tangent to the Sun at the central pixel of SOT/SP FOV, located at $(-107'', -488'')$ in heliocentric coordinates, where the Cartesian reference system employed in the extrapolation is centred. In these coordinates, the uniform spatial resolution of the extrapolated vector magnetogram is $0.32''$ in both directions.

same distribution for the normal field component at the boundaries (see, *e.g.*, Metcalf *et al.*, 2008). Broadly speaking, this is due to non-magnetic forces at photospheric levels, although a clear understanding of how this eventually affects the total energy of the extrapolated field has not yet been reached. One possibility to improve the compatibility between the force-free assumption (that is used in extrapolation methods) and the non-force-free nature of the measurements (that are used as boundary conditions) is to modify the measurements. This operation, called preprocessing, changes the local values of the vector magnetogram in order to better fulfil some global, necessary constraints that a force-free field must obey (Molodenskii, 1969; Aly, 1989). The preprocessing method that we used (Fuhrmann, Seehafer, and Valori, 2007; Fuhrmann *et al.*, 2011) keeps the modifications of measured values within given limits, ideally of the order of local measurements' errors. In the application described in this paper, preprocessing was allowed to change the value of the magnetic field in each pixel of at most ± 150 G (gauss) on B_x and B_y , and of ± 50 G on B_z (horizontal and vertical field components, respectively). The latter is a relatively modest value, especially considering the large component-mixing at such latitudes (around -27°). As a result of preprocessing, the three components of the normalised net force on the magnetogram (Metcalf *et al.*, 2008) are decreased from $(0.02, -0.03, 0.39)$ to $(0.007, -0.008, 0.017)$.

The resulting vector magnetogram employed as the boundary condition for the extrapolation is shown in Figure 1. We note that the FOV of SOT/SP did not cover the whole AR,

as can be seen in Figure 4b, where the LOS component of the SOT/SP vector magnetogram is overlaid on the LOS magnetogram of MDI. In particular, some of the negative flux concentrations on the east side, as well as a compact positive one in the south are excluded from the vector magnetogram.

3. Extrapolation Methodology and its Application to AR 11024

The magneto-frictional method is a numerical technique to find solutions of the nonlinear force-free equations,

$$\nabla \times \mathbf{B} = \alpha \mathbf{B} \quad \text{with } \nabla \cdot \mathbf{B} = 0, \quad (1)$$

for a given distribution of magnetic field at the boundaries of the extrapolation volume. Our implementation of the method consists of a pseudo-temporal evolution that diffuses out of the computation box Lorentz forces and errors in $\nabla \cdot \mathbf{B}$, until a force-free state is reached that matches the required vector field at its bottom boundary (Valori, Kliem, and Keppens, 2005; Valori, Kliem, and Fuhrmann, 2007; Valori *et al.*, 2010). Typically, the employed information on the bottom boundary consists of the vector magnetogram that is either measured or extracted from a three-dimensional numerical solution of Equation (1) in the case of test fields. The field on the lateral and top boundaries is prescribed implicitly so to allow flux and electric currents through them.

In a series of previous papers we have shown that, if the magnetic field on the bottom boundary is compatible with a force-free solution, then the magneto-frictional method reconstructs accurately the sought solution of Equation (1) both in its integral (energy, magnetic helicity, *etc.*) as in its local properties (like, *e.g.*, current sheets). In particular, we examined configurations containing a flux rope with an average twist of $\approx 2\pi$ (Valori, Kliem, and Keppens, 2005; Valori *et al.*, 2010), and found that the reconstructed flux rope reproduces the average twist to within 97% to 99% accuracy, depending on the particular equilibrium considered (see, *e.g.*, Table 3 in Valori *et al.*, 2010). Similarly, the magnetic helicity of the extrapolated field is reproduced with a 5% error at most, and the magnetic energy within just 1%. It is also worth noticing that the complexity of the magnetic field structure was found not to be an obstacle for extrapolation. For instance, the two complementary examples in Valori, Kliem, and Keppens (2005) and Valori *et al.* (2010) dealt with flux ropes with and without return currents, respectively, and were successfully reconstructed in both cases (see also Valori, Kliem, and Fuhrmann (2007) for an example of extrapolation of a topologically simpler field). Also the presence of specific magnetic structures, like bald patches (Titov, Priest, and Demoulin, 1993) and hyperbolic flux tubes, were reproduced with success (within, *e.g.*, an error of at most 2% in the height of an hyperbolic flux tube). Applications of our code to measured magnetograms are included in Metcalf *et al.* (2008), Schrijver *et al.* (2008), and DeRosa *et al.* (2009).

In the application presented in this paper, the extrapolation grid is given by $293 \times 424 \times 321$ nodes, with a uniform resolution of $0.32''$. The analysis volume, \mathcal{V} , used for the computation of global metrics, like magnetic helicity and energy, is given by the whole grid including the photospheric layer, but excluding the outer twelve grid layers on each of the non-photospheric (*i.e.*, lateral and top) sides (see Valori, Kliem, and Fuhrmann (2007) for details on the method).

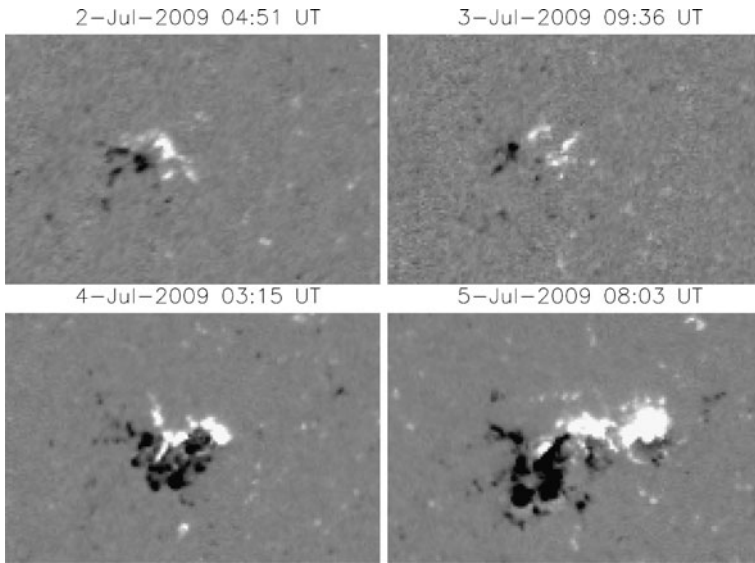
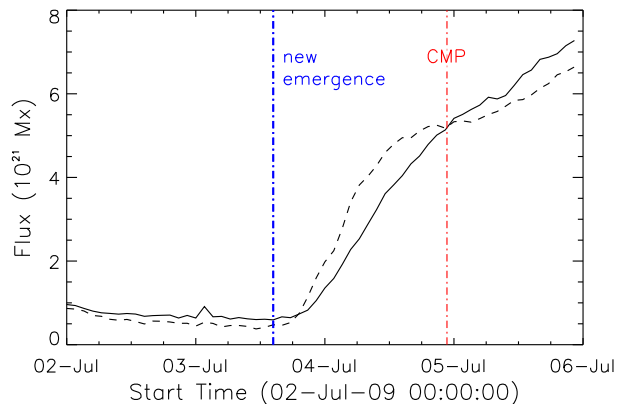


Figure 2 Time evolution of the LOS magnetogram from MDI, saturated at 300 G, with positive/negative polarities represented in white/black. See the attached electronic material for a movie of the evolution (saturated at 500 G).

Figure 3 Time evolution of the emerging positive (solid line) and negative (dashes) magnetic flux in the entire AR. The start of the main emergence phase and the time of the central meridian passage (CMP) are indicated by vertical lines.



4. Observations

NOAA AR 11024 was a southern hemisphere region, at about -27° of latitude, with positive leading polarity, and it was globally bipolar both in its emergence and decay phases (see Figure 2 and the supplementary electronic material for a movie of the whole evolution). In the previous rotation, no sign of activity was present at that latitude. When it rotated over the east limb on 29 June 2009, the emerging AR was a tiny bipole, oriented in the same way as at the end of its growing phase, close to the western limb, when the field was essentially axial again (as inferred from the absence of magnetic tongues). Therefore, the early phase of emergence was likely to be formed by the top of axial field of the emerging flux tube.

The AR remained relatively quiet until, at the end of 3 July 2009, suddenly the main phase of emergence occurred (Figure 3). At this time, the region was close to the central

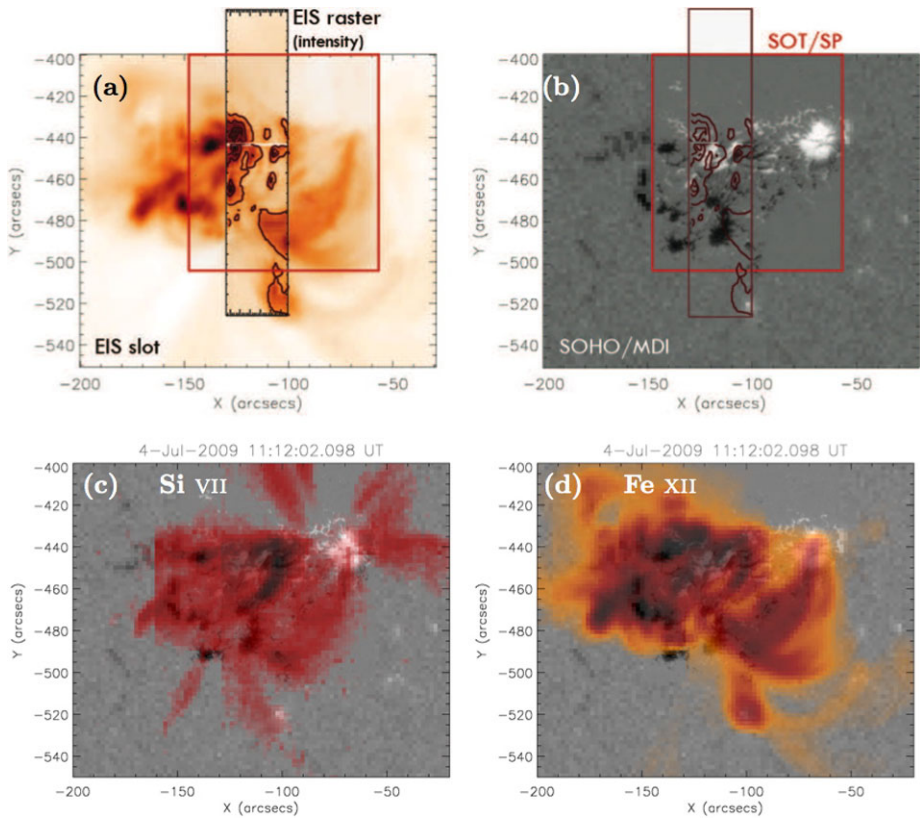


Figure 4 (a) Overlay of the intensities in Fe XII line of EIS raster on the EIS slot image (the SOT/SP FOV is outlined with a red square). (b) Overlay of the SOT/SP (LOS component, bordered by the red square) on the MDI LOS magnetogram. Intensity isocontours of EIS raster are overlotted with dark brown lines. (c) and (d) are EIS images in the Si VII and Fe XII lines from an EIS 40'' slot raster captured between 11:52:26 and 11:55:52 UT, overlaid on image (b). In both cases the EIS scan is displayed using a reversed colour scale with the strongest emission appearing dark and the weakest emission bright. The contrast of both images has been adjusted so that the strong emitting feature is enhanced.

meridian. The rapidly emerging flux had the same magnetic configuration as the pre-existing AR, *i.e.*, a positive leading polarity. However, the tilt of the new bipolar flux emergence was significantly higher than in the pre-existing region, which implies that an important azimuthal field component was emerging at this time. As a result, clear magnetic tongues were formed: The leading (positive) polarity of the emerging flux was observed to extend along the northern side of the following (negative) polarity, indicating that the flux had negative helicity (see the bottom two panels of Figure 2 and López Fuentes *et al.*, 2000). In between the main accumulations of the leading and following polarities, small bipolar flux regions were observed to emerge (see Figure 4b), which are believed to be a photospheric signature of the so-called serpentine field (see Section 1). The emerged polarities either cancelled with the pre-existing field of opposite sign, or underwent coalescence with the like-polarity. The emergence of bipoles in the core of the AR lasted until 7 July 2009, when also the magnetic tongues were completely retracted. After the retraction of the magnetic tongues, the AR had

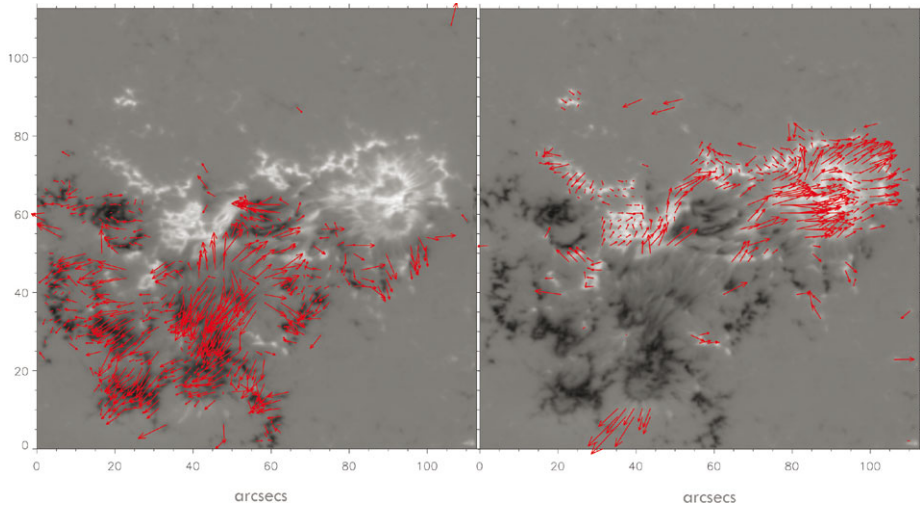


Figure 5 Photospheric flow horizontal velocities on negative (left) and positive (right) polarities. Red arrows represent velocities up to 3 km s^{-1} with the background being the average image with positive (white) and negative (black) polarities (saturated at $\pm 2500 \text{ G}$). The flow maps were derived from LCT analysis in the interval 12:00 to 13:00 UT employing a FWHM correlation window of $3''$.

again the structure of a large-scale bipole which got progressively dispersed by losing flux (observed as moving magnetic features almost all around the sunspots).

Quantitatively, the emergence history is summarised by Figure 3, where the flux evolution over four days around the major flux emergence event is shown. Central meridian passage of the AR occurred by the end of 4 July. The main flux emergence begins when the region is in the eastern hemisphere (end of 3 July) and the polarities are imbalanced with more negative than positive flux detected. This is due to a projection effect produced by the presence of a significant horizontal field component, which in the eastern (western) hemisphere results in the following (leading) polarity of the AR dominating the flux budget (Green *et al.*, 2003).

At the time of the main emergence, the AR was observed also by *Hinode/SOT*. Figures 4c and 4d show images of the EIS/Si VII and EIS/Fe XII lines, probing the plasma at transition-region and coronal temperatures, on 4 July 2009. Several features are visible, among which the western connection of the leading polarity 1 with the negative polarity 2 (*cf.* Figure 1), and a strong emission in the core of the AR at about $x \simeq -110''$, well visible in the Si VII line of Figure 4c. We also notice a feature with strong emission on the south, approximately at $(-100'', -520'')$ in Figure 4d, located in correspondence to a positive polarity concentration (visible in the MDI LOS magnetogram but outside the SOT/SP FOV). This feature appears to be disconnected from the leading polarity, and is probably a transient microflare occurring at the time of rastering.

Associated with the main phase of the emergence there is a global flow that pushes southwards the negative polarity, and westwards the positive one. This AR-wide pattern in the flow is clearly shown by the LCT flow map in Figure 5. At smaller spatial scales, it also shows the motions of the emerging bipoles (see also the attached online SOT/NFI movie). These motions are related to the magnetic configuration described in Section 6.

Finally, the flare spectrum reconstructed by the *Reuven Ramaty High Energy Solar Spectroscopic Imager* (RHESSI) shows several peaks in the considered emergence phase, all in

the thermal range.² In particular, three peaks in the 3–6 and 6–12 keV ranges are found, all approximately located at (−100′, −445′) in heliographic coordinates, which are co-temporal with the SOT/SP scan (at 12:09, 12:13, and 12:24 UT). The location of the HXR emission is again in the region of the strong emission in the Si VII image of Figure 4c noted above.

The observations presented in this section describe the emergence process of the AR in its photospheric and low-coronal signatures. We can now turn to nonlinear force-free extrapolation, which provides a snapshot of the three-dimensional magnetic field at the time of the main emergence, in order to put these observations in the context of the magnetic field structure.

5. Global Analysis of the Reconstructed Field

The magneto-frictional code described in Section 3 was applied to the vector magnetogram obtained as reported in Section 2. In this section we proceed to the analysis of the reconstructed coronal field and its interpretation in the context of flux emergence.

5.1. Solution Consistency

The extrapolated field is an approximate solution of the force-free equation. A wide-spread measure of the degree of force-freeness of numerical solutions in a volume \mathcal{V} is the fraction of the electric current in the volume that is perpendicular to the magnetic field:

$$\sigma_J \equiv \frac{\int_{\mathcal{V}} d\mathcal{V} |\mathbf{J}_{\perp}|}{\int_{\mathcal{V}} d\mathcal{V} |\mathbf{J}|}, \quad \text{or} \quad \sigma_J \equiv \frac{\sum_i |\mathbf{J}_i| \sigma_i}{\sum_i |\mathbf{J}_i|}, \quad \text{where } \sigma_i = \frac{|\mathbf{J}_i \times \mathbf{B}_i|}{|\mathbf{J}_i| |\mathbf{B}_i|}, \quad (2)$$

where the second expression is the equivalent traditional definition of σ_J as current-weighted, average sine-angle between current and magnetic field (Wheatland, Sturrock, and Roumeliotis, 2000; sometimes the same quantity is referred to as CWsin). The solenoidal property is quantified by the average, $\langle |f_i| \rangle$, over the grid nodes of the fractional flux,

$$f_i = \frac{\int_v dv \nabla \cdot \mathbf{B}_i}{\int_{\partial v} dS |\mathbf{B}_i|}, \quad (3)$$

through the surface ∂v of a small volume v including the node i . Equation (3) tests the integral form of the magnetic flux conservation in the vicinity of the grid node i . We note that, even at a null point, f_i is finite: $f_i = (\lambda_1 + \lambda_2 + \lambda_3) / (|\lambda_1| + |\lambda_2| + |\lambda_3|)$, where $\lambda_1, \lambda_2, \lambda_3$ are the eigenvalues for the Jacobian matrix of the magnetic field.

The reconstruction of the coronal field discussed here has $\sigma_J = 0.11$ and $\langle |f_i| \rangle = 7 \times 10^{-8}$ (in the analysis volume \mathcal{V} that includes the photosphere). Such figures are considered to be small in applications to measured vector magnetograms; therefore, the reconstruction is sufficiently force- and divergence-free.

²The quicklook of RHESSI data is available at the web-address <http://sprg.ssl.berkeley.edu/tohban/browser/>.

5.2. Helicity and Free Magnetic Energy

We compute the relative magnetic helicity following the works of Berger and Field (1984) and Finn and Antonsen (1985), where the helicity of the NLFFF is defined with respect to that of the potential one having the same distribution of normal field at the boundaries of the considered volume. The latter condition is necessary in order to obtain a relative magnetic helicity that is gauge-independent. In the application to the extrapolated field we need to consider that the computational volume is not large enough to neglect fluxes through lateral and top boundaries. Besides the size of the numerical domain, there are complications due to the fact that strong flux concentrations are present also close to the edges of the vector magnetogram, that the magnetogram is flux unbalanced (with 15% excess of positive flux within the SOT/SP FOV), and that open boundary conditions are employed on the lateral and top boundaries during the extrapolation which allow fluxes to go through them. Therefore, we compute the reference potential field, $\mathbf{B}_p = -\nabla\phi$, to be employed in the helicity computation by solving numerically the Laplace equation for the scalar potential, ϕ , with Neumann boundary conditions (given by the normal components of the extrapolated magnetic field on all six boundaries of the analysis volume). In this way we ensure that the obtained value of helicity is indeed gauge-independent, and that the energy of the potential field can be meaningfully compared with the energy of the NLFFF.

The practical computation of the helicity value follows DeVore (2000). He proposed to use a gauge for the vector potential, \mathbf{A} , that is different from the one traditionally used ($\text{div}\mathbf{A} = 0$). This is permitted, as the employed expression for the relative helicity is gauge invariant. This gauge simply corresponds to the vanishing of the vertical component of the vector potential, which greatly simplifies its computation. The main difference with DeVore's work is that we extend his method to a finite volume (with non-vanishing magnetic field on the lateral and top boundaries). The vector potentials of the potential field and of the NLFFF are affected by the lateral and top boundaries. Since the tangential components of the vector potentials on these boundaries are not equal, the complete formula of relative helicity (Finn and Antonsen, 1985) needs to be computed. The explicit formulae used in the computation are derived in the [Appendix](#).

With this method we find a relative helicity value of about $-1.1 \times 10^{42} \text{ Mx}^2$, hence opposite in sign to the statistical hemispheric rule, but in agreement with the observed magnetic tongues. In units normalised by the magnetic flux (or equivalent number of turns for a flux rope), the helicity value is -0.05 , which is in the range of values found in other ARs by summing the photospheric helicity flux (see, e.g., Démoulin and Pariat (2009) and references therein). We finally notice that the extension to finite volumes is essential in the considered case, since a direct application of the formulae by DeVore (2000) would lead to a positive value of the relative magnetic helicity, *i.e.*, would be in contradiction with the sign of helicity as deduced from the observed tongue structure and from the negative magnetic shear (see, e.g., Figures 6 and 7).

The total magnetic energy in the considered volume, defined as $\int_V dV B^2/2$, is 2.1×10^{33} erg, corresponding to 13% more energy than in the potential field with the same distribution of normal field at the boundaries. Therefore, the extrapolation estimates in 2.8×10^{32} erg the free energy available in the considered volume to power coronal activity. This is comparable to the energy liberated in an X-class flare. Still, the observed activity level of the AR showed only B-class flares (with a C-class flare the following day).

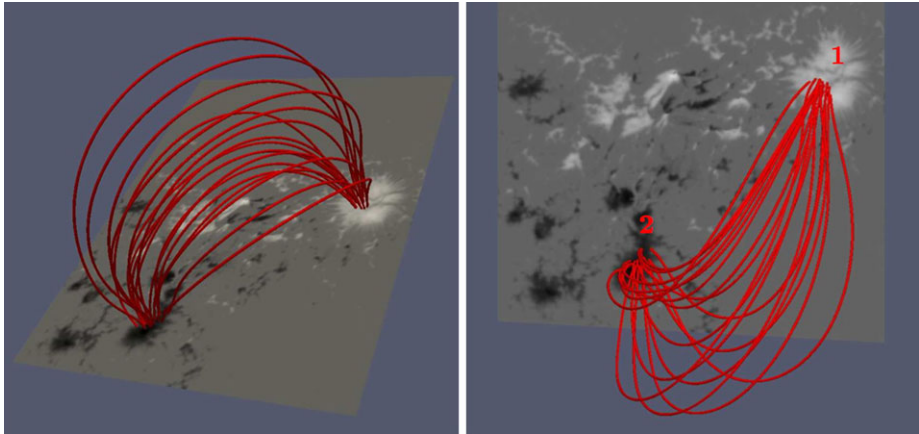


Figure 6 Field lines starting inside the umbra of the leading polarity (1), in three-dimensional view (left) and in projection on the plane of the sky (right). The photospheric vertical magnetic field B_z is shown in grey scale on the bottom plane (black: negative; white: positive).

6. Structure of the Three-Dimensional Magnetic Field

In this section the structure of the extrapolated magnetic field is analysed, proceeding from larger to smaller scale.

6.1. Large Scale: The External Part of the Emerged Flux System

Figure 6 shows how the leading polarity (1) is connected with the southern negative one (2) with field lines travelling high up in the corona. This connection forms the external connectivity envelope which corresponds to the first emerged sunspot pair. This group of field lines, viewed in projection on the plane of the sky, correspond to the south-west loops in the EIS/Si VII and EIS/Fe XII images shown in Figures 4c and d (of course, only for that part of the AR which is actually covered by SOT/SP measurements and, hence, extrapolated).

Next, if the total flux in the whole area is considered in the computation of the tilt angle, then a value of about 25° is found (Schlichenmaier *et al.*, 2010). However, taking as tilt angle of the AR the angle formed by the equator with the line connecting the leading polarity (1) to the negative polarity (2), we find a value of about 45° (Figure 6), a huge value, about six times larger than what is expected from Joy's law (Dasi-Espuig *et al.*, 2010). The large tilt of the sunspot group as a whole is reflected in the flow patterns derived by LCT (Figure 5): The flow pattern associated with the leading polarity is globally in the west direction, whilst that on the following polarity is clearly pointing southwards. Referring to the history of the AR as shown by the MDI movie (see Section 4 and the attached electronic material), this organised flow belongs to the main phase of the emergence (after the blue vertical line in Figure 3). Such a flow pattern, together with the associated tilt of the sunspot axis, might be the result of the emergence of a non-planar flux tube.

6.2. Intermediate Scale: Connection Between Magnetic Tongues

The complex polarity distribution in the core of the AR makes it difficult to guess the magnetic connectivity of the emerged flux from the MDI and SOT/NFI time series only. Extrapolation can in this case provide the missing information. As an example, let us consider the

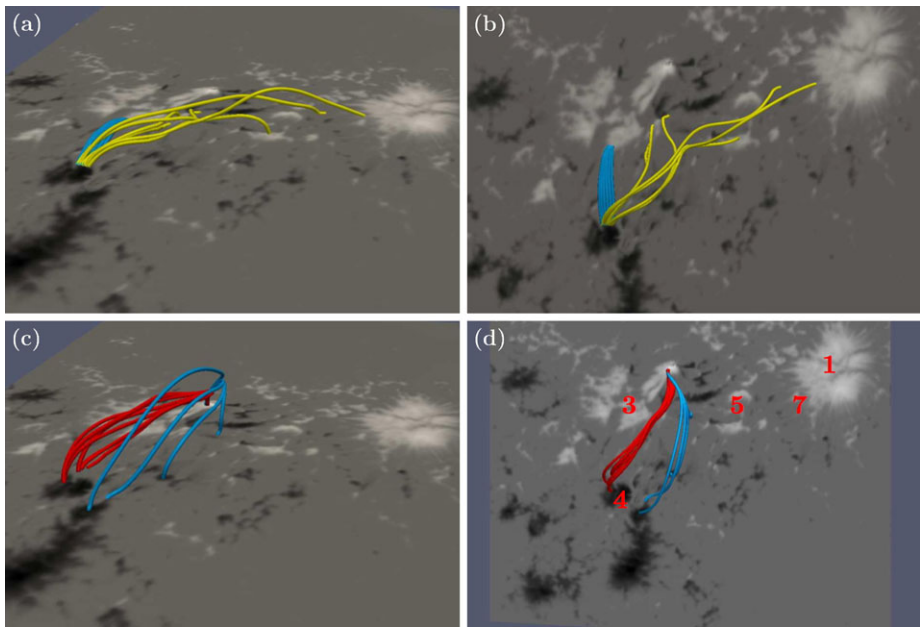


Figure 7 Connectivity of the negative polarity 4. Top row: Selected field lines (yellow) connecting the polarity 4 with the emergence region, in (a) three-dimensional view, and (b) orthogonal projection. Bottom row: Field lines starting at the northern part of polarity 3 (red) connected with the southern polarity 4, in (c) three-dimensional view, and (d) in projection on the plane of the sky. In all four panels, the blue field lines are potential field lines drawn from the same locations as the red and yellow ones determined from a NLFFF extrapolation.

magnetic connectivities of the compact negative polarity 4 (labelled in Figure 7d). Despite its proximity to polarity 2 (southward of polarity 4), Figures 7a and b show that the magnetic connectivity of polarity 4 is almost entirely disconnected from the leading polarity 1, and it spreads over a relatively wide area on the positive polarity with an extension up to about 10 Mm in height. These field lines connect to the area of more dispersed polarity in the core of the AR (polarity 5, mostly), extending up to the periphery of the leading polarity 1 (in particular polarity 7), with clearly dipped, relatively low-lying field lines. These dips are partly overlying the area of flux emergence, and they are the first indication of a sea-serpent configuration.

Such an indication is entirely absent in the potential extrapolation. Here field lines starting from polarity 4 (starting at the same locations as the yellow lines and shown in blue in Figures 7a and b) form a compact bundle connecting to the northern large positive polarity (3).

In the proximity of the polarity 4, a second group of field lines, best visible if drawn from the northern part of the positive polarity 3 (Figures 7c and d), connects to the negative polarity 4 with a moderately negative twisted configuration overlaying the photospheric inversion line (hereafter: PIL). Projected on the plane of the sky, this group of field lines has approximately the same location and shape of the bright loop (dark in reversed colour table) visible in the EIS/Si VII image of Figure 4c at $x \simeq -110''$ and extending from $y \simeq -470''$ to $y \simeq -440''$.

Compared to the corresponding potential field lines (shown in blue in Figures 7c and d), field lines in the nonlinear force-free extrapolation (in red) are more compact. The departure

from the potential ones in azimuth is an indication of their shear. An even larger magnetic shear is present for the yellow field lines (Figures 7a and b). Both indicate a negative magnetic helicity.

The elongation of the positive polarity extending from the positive sunspot along the PIL recalls the formation of magnetic tongues during the late stage of a flux rope emergence (Démoulin and Pariat, 2009; Archontis and Hood, 2010). On the other hand, the fact that such a relatively wide extension of positive flux is largely connected with a compact negative one implies an asymmetry of the magnetic tongues (whilst only symmetric cases have been analysed in models and simulations so far). Still, the magnetic connectivity that we find at this scale confirms the nature of the magnetic tongues as was argued in Section 4 on the ground of photospheric observations only.

6.3. Sea-Serpent Emergence

Previous works have concluded that during the emergence the flux rope acquires a serpentine shape that, at a given time, is still partly below the photosphere, whilst the higher coils have already emerged (*e.g.*, Pariat *et al.* (2004) and references therein). Here we want to further test this model by combining information from the horizontal flow and the structure of the NLFFF.

The photospheric signature on the vertical field of a sea-serpent type of emergence is given by a series of magnetic flux concentrations of alternating polarity (see Figure 8 in Strous and Zwaan (1999) and Figure 12 in Vargas Domínguez, van Driel-Gesztelyi, and Bellot Rubio (2010) for cartoons of the process). Associated with them, a very specific flow pattern is present: an emerged segment of the flux rope arches as sheared Ω -loops over an inversion line from where the flow is divergent; on the contrary, where the flux rope is still below the photosphere, the photospheric flux concentrations are separated by an inversion line where the flow is convergent, and above which U-loops are formed (depending on the stage of emergence, bald patches may be present where the field lines are tangent to the photosphere). We call PIL_{Ω} the first type of – portions of – inversion lines, and PIL_{U} the second ones. Therefore, in order to prove that we are indeed in the presence of a sea-serpent emergence, this peculiar alternation of polarities with specific flow patterns around inversion lines and its associated connectivity must be verified.

As an example, we consider the sub-domain of the emergence area shown in Figure 8, where the labelling of the inversion lines was done in accordance to the flow direction in their neighbourhood, as deduced from the LCT analysis. In the first place, we note the presence of alternating types of PIL which separate the polarities involved in the emergence, as follows. Both PIL_{Ω} s in Figure 8 are surrounded by diverging motions if we exclude a small converging region located on the negative polarity of the right PIL_{Ω} (close to the PIL_{Ω} symbol), whilst the PIL_{U} is surrounded by converging motions if we exclude some diverging motions also on the same negative polarity. Indeed, in both cases, the excluded motions are located in weak magnetic fields, which are likely to be unresolved and where the LCT has difficulties to follow the flux tube motions. The attached SOT/NFI movie visually supports the calculated diverging/converging motions at the $\text{PIL}_{\Omega/\text{U}}$.

Which types of field line do we find close to them? Starting from the leading polarity 1 and proceeding eastward, we meet first an emerged segment of the flux rope (rightmost group of yellow field lines in Figure 9) arching over a PIL_{Ω} inversion line separating polarities 8 and 7, and where divergent flows are present. Similarly, the next PIL_{Ω} curve, again characterised by diverging flows, is also located below a dome of emerging field lines (the left group of yellow field lines connecting polarities 6 and 5 in Figure 9).

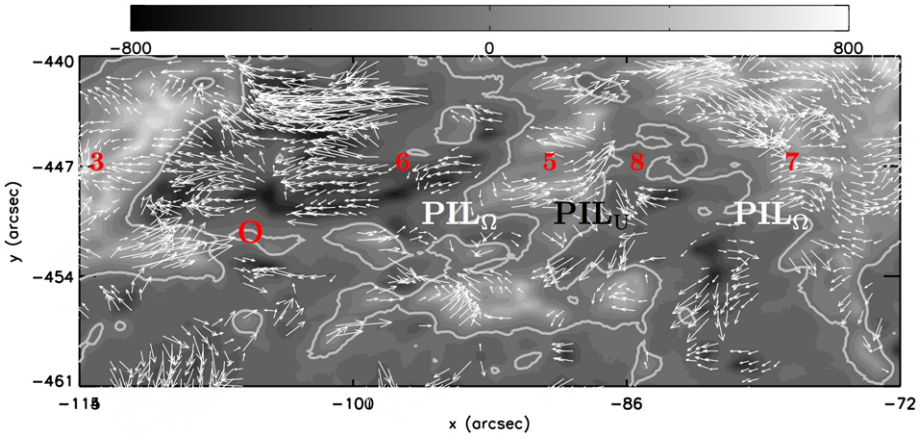


Figure 8 Vertical magnetic field component in the sea-serpent region (in grey scale, *cf.* Figure 1) with arrows representing the LCT flow map obtained with a $1''$ FWHM correlation window. The length of the arrows is proportional to the magnitude of the horizontal velocities, ranging between 0.2 and 3.9 km s^{-1} . The average velocity in x and y directions within the FOV (equal to 0.24 and 0.13 km s^{-1} , respectively) are subtracted from the flow map in order to enhance motions relative to the PILs. PIL_Ω and PIL_U indicate the inversion line parts which have Ω - and U -loops above them, respectively. The red circle is the projected approximate position of the null point discussed in Section 6.4.

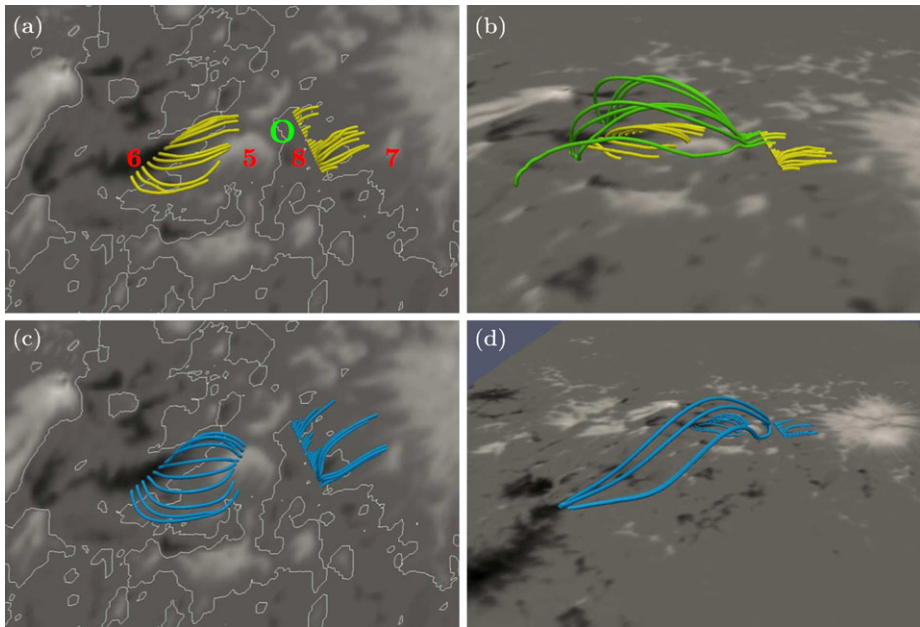


Figure 9 (a) The emerging sea-serpent above the PIL_Ω s of Figure 8 imaged with yellow field lines, in orthogonal projection. The vertical field B_z is shown in grey scale in the background, together with the PIL (in white). The green circle indicates the portion of the PIL_U where bald patches are found, and from where the green field lines of the right panel start. (b) Perspective from a southern point of view of the magnetic configuration above the PILs. Green field lines are computed from points lying $0.5''$ above the bald patch at the PIL_U (*cf.* Figure 8), whilst the yellow lines are the same than in the left panel. (c) As for panel (a) but for the potential field. (d) As panel (b) but for the potential field and a larger field of view.

In between these two PIL_Ω segments lays a PIL_U one, *i.e.*, characterised by converging flows, which separates polarities 5 and 8 that are not directly connected by field lines. Instead, the field lines starting right above the PIL_U connect the external polarities of the two emerging flux regions at its sides as shown by the green field lines in Figure 9b. These field lines start from the northern segment of the PIL_U where bald patches are present (indicated in Figure 9a by a green circle). Together with their associated separatrices, bald patches are preferred locations for the formation of current layers, so there reconnection can occur (Pariat, Masson, and Aulanier, 2009; Archontis and Hood, 2009).

In summary, we find confirmation of the sea-serpent emergence picture: as a result of the converging motions associated with the emergence on both PIL sides, field lines are dragged toward the PIL_U inversion line, where they reconnect. The photospheric signature of this process is the mutual cancellation of magnetic features of opposite sign at PIL_U , corresponding to submerging small reconnected loops (see the attached online SOT/NFI movie). Conversely, the reconnected field lines above the PIL_U encompass with longer connectivity both domains of emergence at its sides.

The corresponding field lines in the potential field are shown in Figure 9c, d. The field lines shown in Figure 9c are similar to those in the nonlinear force-free extrapolation, with the only exception that the eastern Ω -loops in the NLFFF are more inclined with respect to the PIL , showing a finite left-hand shear of the emerging magnetic field. Hence, this comparison shows that also at the serpentine scales we find the same helicity signature as on larger scales, confirming the conjecture that small-scale emergence within an AR is the result of the fragmentation of a single, sub-photospheric structure.

In summary, we recognise the emergence process in the core of the AR as a sea-serpent emergence. We recall that what we have described above is only one example of an emergence process inside the AR, since this type of process happens at several locations at a given time (see the online attached SOT/NFI and MDI movies).

6.4. An Example of Interaction Between the Sea-Serpent and the Large-Scale Fields

The easternmost PIL in Figure 8 (between polarities 3 and 6, *cf.* also Figures 10d and 11d) divides opposite polarities which are magnetically connected with each other. This leftmost positive polarity was already recognised in Section 6.2 to be part of the magnetic tongues, and it does not belong to the emerging sea-serpent any more (see the red field lines in Figures 10a and 11a, which are the same as in Figures 7c and d). Flux is emerging at its right side (yellow field lines in Figures 10a and 11a, similar as in Figure 9).

In between the emerging flux and the tongue structure, a null point is found with four types of connectivity in its surroundings (Figures 10b and 11b), at a height of $\approx 1.6''$. A null point is known to be a preferred location for reconnection and so for magnetic energy release. Indeed, the location of the null point in projection, marked by a red circle in Figure 8, lies inside the area of the strongest thermal emission registered by RHESSI at the time of the SOT/SP spectropolarimetric scan as mentioned in Section 4.

No null point is found in the potential field extrapolation. Indeed, the position of a null point is affected by the magnetic field created by the coronal currents. In some cases, especially if it is located at low heights, a null point can simply cross the lower boundary as the coronal currents are modified. An example, where the null point is present only for coronal currents that are large enough, is shown in Figure 4a of Démoulin, Hénoux, and Mandrini (1994). Still, potential field lines have a quadrupolar set of connections (Figures 10c and d), showing that the magnetic connectivity is similar in both cases (the main difference being the amount of magnetic shear). Indeed,

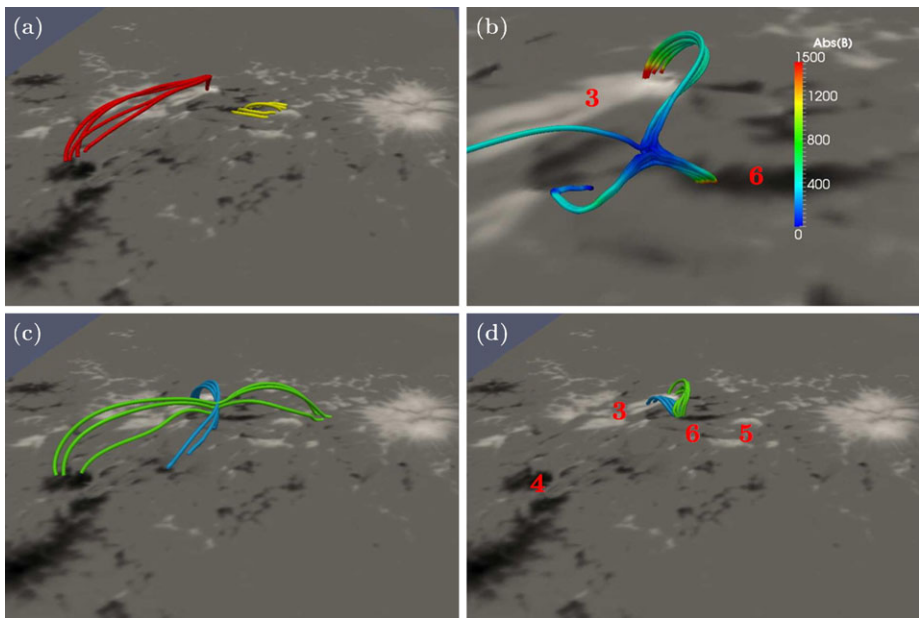


Figure 10 (a) Sheared field lines connecting the newly emerged polarities (yellow) and magnetic tongues (red; the associated potential field lines are shown in Figure 7c, d). (b) Reconnecting field lines in the proximity of a null point (close-up), where the colour code indicates the magnitude of the magnetic field along the field lines. (c) Reconnected field lines, south of the null point (green) and their counterpart in the potential field (blue). (d) Reconnected field lines, north of the null point (green) and their counterpart in the potential field (blue). By considering that the magnetic extrapolation provides approximately the magnetic configuration at the corresponding time of the magnetic evolution, the four panels depict the evolution of the new flux from its emergence to its reconnection to the large-scale field: field lines of the emerging flux connecting polarities 5 and 6 (in yellow in (a)) are pushed toward the pre-existing field lines connecting polarities 3 and 4 (in red in (a)). Reconnection takes place at the null point (b), forming an upper system of long-range and undulating field lines (c, green) linking polarities 4 and 5, and shorter connections (d, green) linking polarities 3 and 6.

the separatrices associated to the null point for the NLFFF are no longer present in the associated potential field, but quasi-separatrix layers remain (Démoulin *et al.*, 1996; Masson *et al.*, 2009). Still similar physics is thought to be operating in both cases, *i.e.*, the formation of a current layer where reconnection occurs.

Assuming that our NLFFF extrapolation provides a time-slice of the magnetic evolution, our interpretation of the flow pattern and magnetic connectivity in this area is the following. The emerging magnetic flux, connecting polarities 6 and 5 and associated with the sea-serpent configuration (yellow lines in Figures 10a and 11a), drags the emerged Ω -loops toward the null point (*cf.* flows in the proximity of the red circle in Figure 8), where they reconnect with the tongue field lines (in red in Figures 10a and 11a). A first group of field lines formed by the reconnection process at the null point connects the adjacent polarities 3 and 6 (green lines in Figures 10d and 11d). The reconnection process also transforms field lines from the tongue structure (in red in Figures 10a and 11a) into field lines connecting the sea-serpent polarity 5 to the negative polarity 4 of the tongue (green lines in Figures 10c and 11c). They have connectivity similar to the yellow field lines shown in Figures 7a and b. Indeed, the above reconnected field lines may later extend up to the leading polarity due to

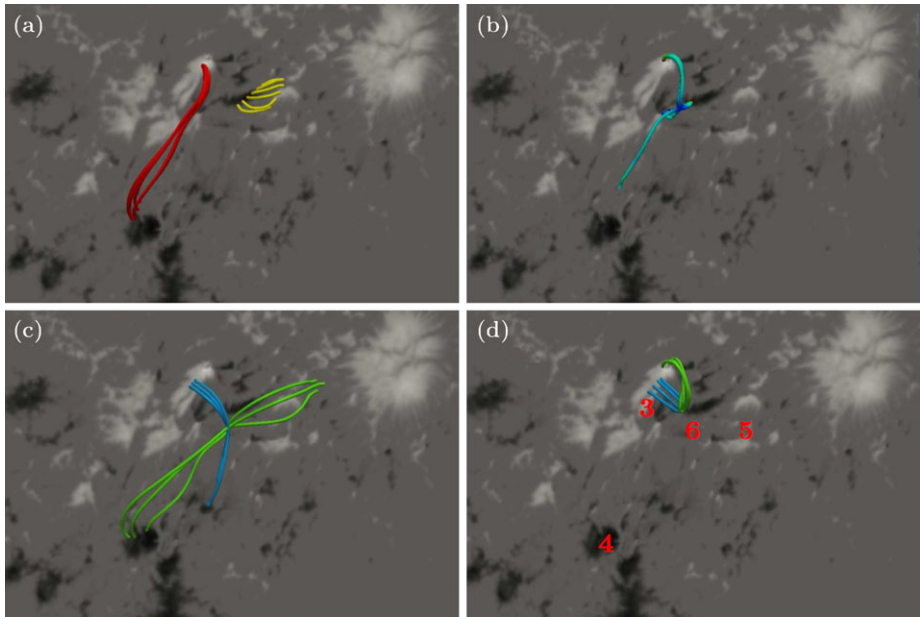


Figure 11 The same group of field lines as of Figure 10a–d, viewed in orthogonal projection.

a second reconnection process at the PIL_U , described in Section 6.3 (*i.e.*, by reconnecting with the western emerging bipole 8–7).

The reconnection scenario that we propose is confirmed by observations with SOT/XRT. The left panel in Figure 12 shows intense emission from a structure with a shape that is similar to the two groups of reconnected green field lines in the right panel of the same figure (the latter are the same field lines as in Figure 11c and d seen together). The strongest emission is found in the vicinity of the null point location. Note that the same structure is visible in SOT/XRT images at different times in the following hours,³ confirming our assumption that the magnetic field structure, obtained from NLFFF extrapolation at one single time, manages to reasonably reproduce the field's connectivity and topology for several hours.

This interpretation describes how the relatively short emerging serpentine field lines are transformed by successive reconnections into long-range field lines connecting the main polarity concentrations of the AR, and thus progressively re-build in the corona a presumed similar connectivity as was present below the photosphere before the emergence. The whole process is basically driven by the advection and compression of the field along the inversion lines generated by the emerging sea-serpent.

Finally, Figures 10d and 11d show the potential field lines corresponding to the reconnected field lines north of the null point. The difference between blue and green field lines indicates the non-potentiality of the field in this area. Note that the LCT flow map of Figure 5 does not support the idea that the green field lines in Figures 10d and 11d are formed by shearing flows, which is in favour of our interpretation involving reconnection at the null point. Similarly, a difference between potential and NLFFF field lines can be seen in Figures 10c and 11c.

³See in the attached electronic material the two XRT movies, spanning the time intervals 11:50–12:29 and 12:33–23:59 UT on 4 July 2009.

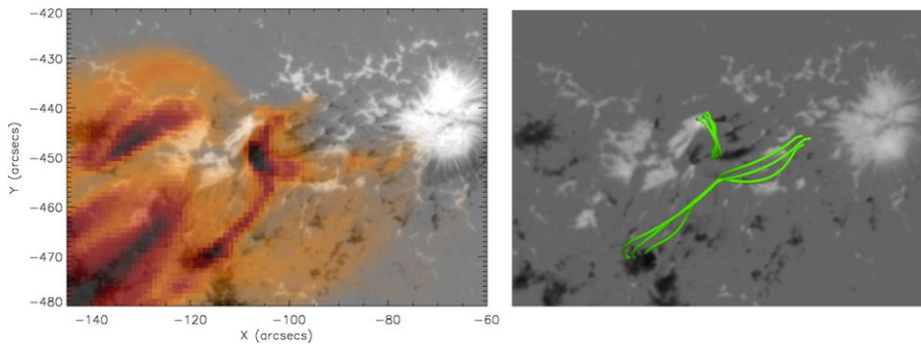


Figure 12 Left: XRT image obtained with the Ti poly filter on 4 July 2009 at 11:52 UT, aligned on the SOT/SP LOS image of 4 July 2009 at 11:58 UT, in reversed colour scale. Right: Same reconnected field lines as the green field lines in Figure 10c, d, projected on the plane of the sky.

The above process is expected to occur at several locations in the emerging flux region as the SOT/NFI time series show emergence and flux cancellation at several locations (see the attached electronic material). For example, emergence is also present southward of polarity 6 (see the attached online SOT/NFI movie). This multipolar photospheric configuration is creating a complex coronal magnetic field with the presence of a null point and separatrices, or more generally, of quasi-separatrix layers (Démoulin *et al.*, 1996). The evolution of such a complex magnetic field implies the formation of current layers, followed by reconnection when a layer is thin enough (Aulanier *et al.*, 2006; Effenberger *et al.*, 2011). Then the above successive reconnections are expected to form the green field lines in Figures 10c and 11c.

As a second example of interaction, the sea-serpent emergence is also present at the inner edge of the leading polarity 1. In Schlichenmaier *et al.* (2010) it is documented that the penumbra, which is still in the formation phase in the morning of 4 July, has a peculiar asymmetric structure, being practically absent on the side of the following polarity. In that paper it is argued that such an asymmetry could be due to flux emergence in the proximities of the eastern side of the sunspot. Our interpretation of the extrapolated field, and of the sea-serpent emergence in particular, confirms their speculation. We also refer the reader to Vargas Domínguez, van Driel-Gesztelyi, and Bellot Rubio (2010) for a detailed analysis of the sea-serpent emergence in this AR at scales comparable with the granulation scale.

6.5. Signatures of Reconnection in Dopplergrams

The EIS raster, starting 21 minutes after the slot image (Figure 4a) and 15 minutes after the SOT magnetogram (Figure 4b), reveals a complex Doppler velocity pattern in the central part of the AR, including dual red- and blue-shifted patterns (marked by dashed contours in Figure 13b). The flows that we measure at the dual patterns are of the order of $\pm 20 \text{ km s}^{-1}$. The bulk of the error is a result of Gaussian fitting/centroid position. We derive a maximum error of 5.8 km s^{-1} on this dual pattern (see Del Zanna (2008) for a discussion of errors in EIS data). This complex flow pattern is in contrast with that of mature ARs where flows are simple: in the AR interior field lines are all red shifted, indicating cooling downflows (Del Zanna, 2008), and at the AR periphery steady outflows are present, interpreted as reconnection between AR field lines and large-scale ones (Baker *et al.*, 2009). These large-scale red-shifts are also present in the core of the studied AR as well as blue-shifts in its northern part (Figure 13b), whilst dual red/blue-shifted patterns stand out from the velocity map (Figure 13b). The large spectral line width visible in Figure 13a at the location of the southern

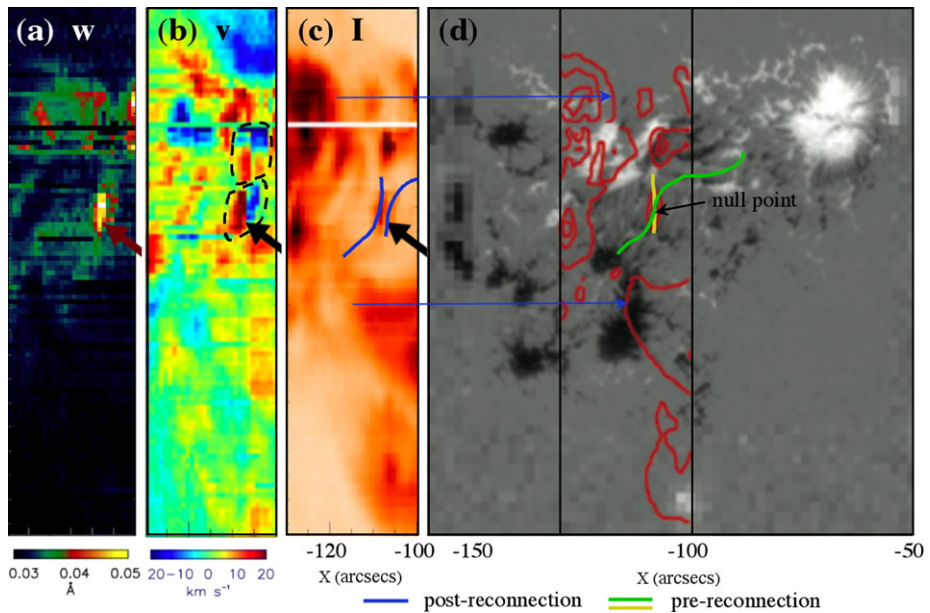
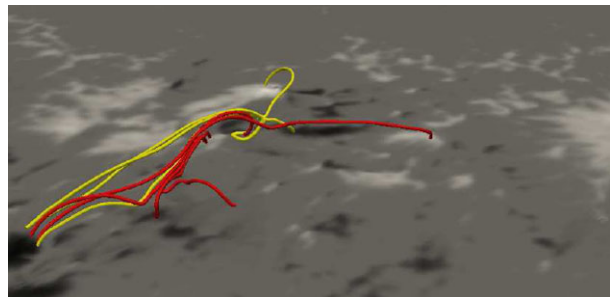


Figure 13 (a) EIS raster, taken between 12:13:55–12:29:44 UT, showing spectral line width in the Fe XII spectral line. (b) Corresponding EIS raster for Doppler velocity. (c) Corresponding EIS intensity raster image. (d) SOT magnetogram with EIS intensity isocontours overlaid (blue arrows show the relationship with panel (c)). In panel (b) the dashed contours indicate the two dual red/blue-shifted patterns discussed in Section 6.5. In panels (a–c) the location of the southern dual red/blue-shifted pattern is pointed out with an arrow. In panels (c, d) the expected post- and pre-reconnection loops are indicated with different colours (see legend at the panel bottom). Field lines in those panels are drawn by hand on the basis of the field lines in the actual extrapolated field (see Figure 14), in order to isolate only the most relevant features.

Figure 14 Selected field lines starting at the null point of Figure 10 (yellow field lines), and at a second null point discussed in Section 6.5 (red field lines).



dual velocity feature (marked by a thick arrow in Figure 13a–c) indicates strong turbulence and/or unresolved flows.

These complex dual patterns are present in the region where field lines connecting the tongues and serpentine field lines co-exist. In particular, a null point is found in the magnetic extrapolation in the vicinity of the southern dual red/blue-shifted pattern (red field lines in Figure 14), at a height of $\approx 1''$. We propose that the dual velocity feature results from magnetic reconnection between field lines connecting the tongues and long serpentine field lines. A couple of such field lines, supported by the NLFFF extrapolation, are shown with simplified shapes in Figure 13d. Other similar field lines are shown by the easternmost yellow

field line in Figure 7b, by the green field lines in Figures 10c and 11c, and more specifically by the red field lines drawn in the vicinity of the null point in Figure 14. The dual velocity feature is interpreted as outflows from the reconnection region located between these field lines. Up/down flows (Figure 13b) are present in the large/small-scale reconnected field lines (Figure 13c), as typically expected in a reconnecting configuration.

A second magnetic null point, whose associated field lines are already shown in Figure 10b and also in yellow in Figure 14, is present in the extrapolation. In correspondence of the second null point, another dual velocity feature is indeed present in EIS data (the northern area marked by dashes in Figure 13b), whilst it has no significant signature in the line-width map (Figure 13a). Figure 14 shows that both nulls are magnetically linked, so both dual velocity features are likely to be related to the same separator-type reconnection.

Although our extrapolation provides a static field, all the connectivity types are present since they are mostly defined by the photospheric magnetogram and the related electric currents. In the specific case of a separator linking two null points, analytical works, confirmed by MHD simulations, demonstrate that boundary motions induce magnetic reconnection at the separator (see, *e.g.*, Longcope and Magara (2004) and references therein). Moreover the magnetic topology deduced from the extrapolated magnetic field permits one to understand the location of flare ribbons (see, *e.g.*, Masson *et al.* (2009) and references therein). An MHD simulation confirms the reconnection at the expected location (null point) as well as the role of quasi-separatrix layers in the temporal evolution of the flare ribbons. More generally, it is the connectivity pattern (quasi-separatrix layers, including separatrices) that determine where current layers and, hence, reconnection will occur when boundary motions are applied (Aulanier, Pariat, and Démoulin, 2005; Effenberger *et al.*, 2011). The summary of all these studies is that the organisation of connectivities in the initial configuration is crucial in determining the location of reconnection, so that magnetic extrapolation is a key tool to understand where reconnection is expected to occur. The more realistic is the magnetic extrapolation of the coronal field, the better the prediction of the reconnection region is expected to be. On the other hand, our NLFFF extrapolation provides a connectivity that is qualitatively matching direct observations from different instruments (slot images from SOT/EIS and XRT) that is compatible with LCT reconstructions of photospheric flow maps (based on SOT/NFI time series) and of a LOS velocity map (from an SOT/EIS Dopplergram). Since observational constraints are, at present, the only test for NLFFF extrapolations of measured vector magnetograms, we have reasonable hopes that the locations of magnetic reconnection, identified above using the extrapolation, are correct.

7. Conclusions

NOAA AR 11024 was observed to emerge as a simple bipole in the quiet Sun at the east limb, underwent the main phase of emergence when it was close to the central meridian, and it had reached a mature bipolar stage by the time it approached the west limb. Therefore, it provides a perfect case study for flux emergence processes. Observations of the line of sight magnetic field show photospheric signatures of the rapid formation of magnetic tongues, indicating a negative helicity configuration, and the emergence of flux in the form known as “sea-serpent”. The serpentine emergence is supported by flow maps obtained by local correlation tracking techniques. On the other hand, EUV observations provide insight in the global structure of the coronal magnetic field (in projection on the plane of the sky).

This interpretation of the photospheric signatures of emergence is confirmed by the reconstruction of the force-free coronal magnetic field above the AR, obtained using the

magneto-frictional nonlinear extrapolation method. The main result of our investigation is the validation, at all the relevant scales, of the current understanding of the flux emergence process. This synthesis is obtained using a reconstruction of the coronal field at a crucial time during the main phase of emergence. In particular we are able to identify the original connections of the sunspot pair, as well as those between the magnetic tongues, and to relate them to EIS multi-temperature observations. At smaller scales, we find evidence that the emergence has indeed the structure of a sea-serpent, and we can relate the serpentine magnetic field to the emergence and flux cancellation processes that are observed in the motion of small magnetic polarities. We identify some of the locations where reconnection occurs in the corona. These successive reconnections transform the short serpentine field lines into long-range connectivity across the whole AR. The signature of such reconnection processes is observed by XRT and by an EIS scan showing localised dual blue- and red-shifted velocity features (with large non-thermal line broadening in one case). All these successive reconnection events eventually lead to the simplified bipolar structure that is observed when the AR reaches the west limb.

Finally, at the time when the main emergence takes place on 4 July 2009, the relative magnetic helicity in a volume about $100''$ high above the measured vector magnetogram is found to be $-1.1 \times 10^{42} \text{ Mx}^2$ (-0.05 in units of magnetic flux), which is in the expected range of values obtained before in other ARs (see, *e.g.*, Démoulin and Pariat (2009) and references therein). The estimated free energy in the same volume is $2.8 \times 10^{32} \text{ erg}$, which could power an X-class flare, whilst only B-class flares were registered in the hours following the measurement of the vector field. In other words, our magnetic extrapolation reconstructs the coronal field during a quiet-time period of the active region.

In conclusion, from a detailed investigation we find agreement between the current interpretation of observed photospheric signatures of the emergence process and the snapshot of the three-dimensional magnetic field structure that is obtained by nonlinear force-free extrapolation. This helps us to obtain a coherent picture of the emergence and evolution of AR 11024 both on large (active-region) and on small (serpentine) scales.

Acknowledgements The authors thank the referee for helpful comments, which improved the clarity of the paper. We thank Etienne Pariat for useful discussions. GV acknowledges the support of K.D. Leka and G. Barnes in providing the Minimum Energy code and help in using it. The research leading to these results has received funding from the European Commission's Seventh Framework Programme (FP7/2007-2013) under the grant agreement no. 218816 (SOTERIA project, www.soteria-space.eu). LvDG acknowledges funding through the Hungarian Science Foundation grant OTKA K81421. MDI data are provided by the SOHO/MDI consortia. SOHO is a project of international cooperation between ESA and NASA. We thank the SOHO and RHESSI teams for their open data policy. *Hinode* is a Japanese mission developed and launched by ISAS/JAXA, collaborating with NAOJ as a domestic partner, and with NASA and STFC (UK) as international partners. Scientific operation of the *Hinode* mission is conducted by the *Hinode* science team organised at ISAS/JAXA. This team mainly consists of scientists from institutes in the partner countries. Support for the post-launch operation is provided by JAXA and NAOJ (Japan), STFC (UK), NASA (USA), ESA, and NSC (Norway). LMG acknowledges funding from the Royal Society and the Leverhulme Trust.

Appendix: Computation of the Relative Magnetic Helicity in a Finite Rectangular Volume

The helicity of a field $\mathbf{B} = \nabla \times \mathbf{A}$ with respect to that of a reference field $\mathbf{B}_p = \nabla \times \mathbf{A}_p$, in a volume \mathcal{V} , is given by Finn and Antonsen (1985)

$$H = \int_{\mathcal{V}} d\mathcal{V} (\mathbf{A} + \mathbf{A}_p) \cdot (\mathbf{B} - \mathbf{B}_p). \quad (4)$$

Since \mathbf{B} and \mathbf{B}_p are solenoidal, the value of H is gauge invariant if

$$(\hat{n} \cdot \mathbf{B})|_{\partial\mathcal{V}} = (\hat{n} \cdot \mathbf{B}_p)|_{\partial\mathcal{V}}, \tag{5}$$

i.e., provided that \mathbf{B} and \mathbf{B}_p have the same distribution of normal field at the boundaries of the volume \mathcal{V} (\hat{n} is the oriented normal to the surface $\partial\mathcal{V}$ of the volume \mathcal{V}). Note that the invariance of the gauge under the above conditions is true for any pair of scalar field Θ, Ψ such that $\tilde{\mathbf{A}} = \mathbf{A} - \nabla\Theta$ and $\tilde{\mathbf{A}}_p = \mathbf{A}_p - \nabla\Psi$, *i.e.*, the gauge does not need to be the same for the two scalar potentials.

Choosing the potential field as the reference one, Equation (5) can be satisfied by $\mathbf{B}_p = -\nabla\phi$, where the scalar potential $\phi(x, y, z)$ is the solution of the Laplace equation

$$\begin{cases} \Delta\phi = 0; \\ -(\partial\phi/\partial n)|_{\partial\mathcal{V}} = (\hat{n} \cdot \mathbf{B}_p)|_{\partial\mathcal{V}}, \end{cases} \tag{6}$$

and $\partial\mathcal{V}$ represents *all* boundaries, not just the photospheric one.

In order to compute H from Equation (4), the vector potentials \mathbf{A} and \mathbf{A}_p must be constructed. We follow the method by DeVore (2000), but we apply it to computations in a finite rectangular volume $\mathcal{V} = (x_1, x_2) \times (y_1, y_2) \times (z_1, z_2)$. Using the freedom in the choice of the gauge, we fix

$$\hat{z} \cdot \mathbf{A}_p = \hat{z} \cdot \mathbf{A} = 0 \tag{7}$$

in \mathcal{V} . Let us consider the vector potential for the potential field first. A direct integration of the x and y components of $\nabla \times \mathbf{A}_p = \mathbf{B}_p$ in the interval $(z_1; z)$ leads to

$$\begin{aligned} A_{p,x}(x, y, z) &= c_x + \int_{z_1}^z dz' B_{p,y}(x, y, z'); \\ A_{p,y}(x, y, z) &= c_y - \int_{z_1}^z dz' B_{p,x}(x, y, z'), \end{aligned}$$

which can be used in the z component to obtain

$$\partial_x c_y - \partial_y c_x - \int_{z_1}^z dz' (\partial_x B_{p,x} + \partial_y B_{p,y}) = B_{p,z}(x, y, z). \tag{8}$$

Using $\nabla \cdot \mathbf{B}_p = 0$ in Equation (8) we derive a condition on the integration vector $\mathbf{c} = (c_x(x, y, z = z_1), c_y(x, y, z = z_1), 0)$,

$$0 = \partial_x c_y - \partial_y c_x - B_{p,z}(x, y, z = z_1). \tag{9}$$

A possible choice for \mathbf{c} that satisfies Equation (9) is

$$\begin{aligned} c_x &= -\frac{1}{2} \int_{y_1}^y dy' B_{p,z}(x, y', z = z_1); \\ c_y &= \frac{1}{2} \int_{x_1}^x dx' B_{p,z}(x', y, z = z_1), \end{aligned}$$

which leads to

$$\mathbf{A}_p = \mathbf{c} - \hat{z} \times \int_{z_1}^z dz' \mathbf{B}_p = \mathbf{c} - \nabla \times \left(\hat{z} \int_{z_1}^z dz' \phi \right) \quad (10)$$

$$= \mathbf{d} + \nabla \times \left(\hat{z} \int_z^{z_2} dz' \phi \right), \quad (11)$$

where \mathbf{d} obeys the same expression as \mathbf{c} , but it is computed at $z = z_2$. Equation (11) has the same form as Equation (4) in DeVore (2000).

With exactly the same integration procedure we can also construct the vector potential for \mathbf{B} with the gauge fixed by Equation (7), obtaining

$$\mathbf{A} = \mathbf{A}_p(x, y, z = z_1) - \hat{z} \times \int_{z_1}^z dz' \mathbf{B}, \quad (12)$$

where the integration constant is fixed by requiring that the transverse components of the two vector potentials at $z = z_1$ are equal, which implies that Equation (5) is satisfied.⁴

The relative magnetic helicity in the finite rectangular volume \mathcal{V} can then directly be computed from Equation (4), using the potential field derived from the scalar potential satisfying Equation (6), one of the equivalent forms in Equations (10), (11), and (12).

References

- Aly, J.J.: 1989, *Solar Phys.* **120**, 19. doi:[10.1007/BF00148533](https://doi.org/10.1007/BF00148533).
- Archontis, V., Hood, A.W.: 2009, *Astron. Astrophys.* **508**, 1469. doi:[10.1051/0004-6361/200912455](https://doi.org/10.1051/0004-6361/200912455).
- Archontis, V., Hood, A.W.: 2010, *Astron. Astrophys.* **514**, A56. doi:[10.1051/0004-6361/200913502](https://doi.org/10.1051/0004-6361/200913502).
- Aulanier, G., Pariat, E., Démoulin, P.: 2005, *Astron. Astrophys.* **444**, 961. doi:[10.1051/0004-6361:20053600](https://doi.org/10.1051/0004-6361:20053600).
- Aulanier, G., Pariat, E., Démoulin, P., Devore, C.R.: 2006, *Solar Phys.* **238**, 347. doi:[10.1007/s11207-006-0230-2](https://doi.org/10.1007/s11207-006-0230-2).
- Baker, D., van Driel-Gesztelyi, L., Mandrini, C.H., Démoulin, P., Murray, M.J.: 2009, *Astrophys. J.* **705**, 926. doi:[10.1088/0004-637X/705/1/926](https://doi.org/10.1088/0004-637X/705/1/926).
- Berger, M.A., Field, G.B.: 1984, *J. Fluid Mech.* **147**, 133. doi:[10.1017/S0022112084002019](https://doi.org/10.1017/S0022112084002019).
- Bernasconi, P.N., Rust, D.M., Georgoulis, M.K., Labonte, B.J.: 2002, *Solar Phys.* **209**, 119. doi:[10.1023/A:1020943816174](https://doi.org/10.1023/A:1020943816174).
- Culhane, J.L., Harra, L.K., James, A.M., Al-Janabi, K., Bradley, L.J., Chaudry, R.A., *et al.*: 2007, *Solar Phys.* **243**, 19. doi:[10.1007/s01007-007-0293-1](https://doi.org/10.1007/s01007-007-0293-1).
- Dasi-Espuig, M., Solanki, S.K., Krivova, N.A., Cameron, R., Peñuela, T.: 2010, *Astron. Astrophys.* **518**, A7. doi:[10.1051/0004-6361/201014301](https://doi.org/10.1051/0004-6361/201014301).
- Del Zanna, G.: 2008, *Astron. Astrophys.* **481**, L49. doi:[10.1051/0004-6361:20079087](https://doi.org/10.1051/0004-6361:20079087).
- Démoulin, P., Pariat, E.: 2009, *Adv. Space Res.* **43**, 1013. doi:[10.1016/j.asr.2008.12.004](https://doi.org/10.1016/j.asr.2008.12.004).
- Démoulin, P., Hénoux, J.C., Mandrini, C.H.: 1994, *Astron. Astrophys.* **285**, 1023.
- Démoulin, P., Hénoux, J.C., Priest, E.R., Mandrini, C.H.: 1996, *Astron. Astrophys.* **308**, 643.
- DeRosa, M.L., Schrijver, C.J., Barnes, G., Leka, K.D., Lites, B.W., Aschwanden, M.J., *et al.*: 2009, *Astrophys. J.* **696**, 1780. doi:[10.1088/0004-637X/696/2/1780](https://doi.org/10.1088/0004-637X/696/2/1780).
- DeVore, C.R.: 2000, *Astrophys. J.* **539**, 944. doi:[10.1086/309274](https://doi.org/10.1086/309274).
- Effenberger, F., Thust, K., Arnold, L., Grauer, R., Dreher, J.: 2011, *Phys. Plasmas* **18**, 032902. doi:[10.1063/1.3565018](https://doi.org/10.1063/1.3565018).
- Finn, J.H., Antonsen, T.M.J.: 1985, *Comments Plasma Phys. Control. Fusion* **9**, 111.
- Fuhrmann, M., Seehafer, N., Valori, G.: 2007, *Astron. Astrophys.* **476**, 349. doi:[10.1051/0004-6361:20078454](https://doi.org/10.1051/0004-6361:20078454).

⁴We note that a solution similar to Equations (9)–(12), with Coulomb gauge of \mathbf{A}_p , was independently found by N. Seehafer and B. Kliem (manuscript in preparation for *Solar Phys.*).

- Fuhrmann, M., Seehafer, N., Valori, G., Wiegelmann, T.: 2011, *Astron. Astrophys.* **526**, A70. doi:[10.1051/0004-6361/201015453](https://doi.org/10.1051/0004-6361/201015453).
- Gary, G.A., Hagyard, M.J.: 1990, *Solar Phys.* **126**, 21. doi:[10.1007/BF00158295](https://doi.org/10.1007/BF00158295).
- Golub, L., Deluca, E., Austin, G., Bookbinder, J., Caldwell, D., Cheimets, G., et al.: 2007, *Solar Phys.* **243**, 63. doi:[10.1007/s11207-007-0182-1](https://doi.org/10.1007/s11207-007-0182-1).
- Green, L.M., Démoulin, P., Mandrini, C.H., Van Driel-Gesztelyi, L.: 2003, *Solar Phys.* **215**, 307. doi:[10.1023/A:1025678917086](https://doi.org/10.1023/A:1025678917086).
- Harra, L.K., Magara, T., Hara, H., Tsuneta, S., Okamoto, T.J., Wallace, A.J.: 2010, *Solar Phys.* **263**, 105. doi:[10.1007/s11207-010-9548-x](https://doi.org/10.1007/s11207-010-9548-x).
- Hood, A.W., Archontis, V., MacTaggart, D.: 2011, *Solar Phys.* **54**. doi:[10.1007/s11207-011-9745-2](https://doi.org/10.1007/s11207-011-9745-2).
- Leka, K.D., Canfield, R.C., McClymont, A.N., van Driel-Gesztelyi, L.: 1996, *Astrophys. J.* **462**, 547. doi:[10.1086/177171](https://doi.org/10.1086/177171).
- Leka, K.D., Barnes, G., Crouch, A.D., Metcalf, T.R., Gary, G.A., Jing, J., Liu, Y.: 2009, *Solar Phys.* **260**, 83. doi:[10.1007/s11207-009-9440-8](https://doi.org/10.1007/s11207-009-9440-8).
- Longcope, D.W., Magara, T.: 2004, *Astrophys. J.* **608**, 1106. doi:[10.1086/420780](https://doi.org/10.1086/420780).
- Longcope, D.W., Fisher, G.H., Arendt, S.: 1996, *Astrophys. J.* **464**, 999. doi:[10.1086/177387](https://doi.org/10.1086/177387).
- López Fuentes, M.C., Démoulin, P., Mandrini, C.H., van Driel-Gesztelyi, L.: 2000, *Astrophys. J.* **544**, 540. doi:[10.1086/317180](https://doi.org/10.1086/317180).
- Luoni, M., Démoulin, P., Mandrini, C.H., van Driel-Gesztelyi, L.: 2011, *Solar Phys.* **270**, 45. doi:[10.1007/s11207-011-9731-8](https://doi.org/10.1007/s11207-011-9731-8).
- Masson, S., Pariat, E., Aulanier, G., Schrijver, C.J.: 2009, *Astrophys. J.* **700**, 559. doi:[10.1088/0004-637X/700/1/559](https://doi.org/10.1088/0004-637X/700/1/559).
- Metcalf, T.R., Leka, K.D., Barnes, G., Lites, B.W., Georgoulis, M.K., Pevtsov, A.A., et al.: 2006, *Solar Phys.* **237**, 267. doi:[10.1007/s11207-006-0170-x](https://doi.org/10.1007/s11207-006-0170-x).
- Metcalf, T.R., Derosa, M.L., Schrijver, C.J., Barnes, G., van Ballegoijen, A.A., Wiegelmann, T., Wheatland, M.S., Valori, G., McTiernan, J.M.: 2008, *Solar Phys.* **247**, 269. doi:[10.1007/s11207-007-9110-7](https://doi.org/10.1007/s11207-007-9110-7).
- Molodenskii, M.M.: 1969, *Soviet Astron.* **12**, 585.
- Moreno-Insertis, F., Emonet, T.: 1996, *Astrophys. J. Lett.* **472**, 53. doi:[10.1086/310360](https://doi.org/10.1086/310360).
- November, L.J., Simon, G.W.: 1988, *Astrophys. J.* **333**, 427. doi:[10.1086/166758](https://doi.org/10.1086/166758).
- Pariat, E., Masson, S., Aulanier, G.: 2009, *Astrophys. J.* **701**, 1911. doi:[10.1088/0004-637X/701/2/1911](https://doi.org/10.1088/0004-637X/701/2/1911).
- Pariat, E., Aulanier, G., Schmieder, B., Georgoulis, M.K., Rust, D.M., Bernasconi, P.N.: 2004, *Astrophys. J.* **614**, 1099. doi:[10.1086/423891](https://doi.org/10.1086/423891).
- Scherrer, P.H., Bogart, R.S., Bush, R.I., Hoeksema, J.T., Kosovichev, A.G., Schou, J., et al.: 1995, *Solar Phys.* **162**, 129. doi:[10.1007/BF00733429](https://doi.org/10.1007/BF00733429).
- Schlichenmaier, R., Rezaei, R., Bello González, N., Waldmann, T.A.: 2010, *Astron. Astrophys.* **512**, L1. doi:[10.1051/0004-6361/201014112](https://doi.org/10.1051/0004-6361/201014112).
- Schmieder, B., Deng, Y., Mandrini, C.H., Rudawy, P., Nitta, N., Mason, H., Fletcher, L., Martens, P., Brynildsen, N.: 2000, *Adv. Space Res.* **25**(9), 1879. doi:[10.1016/S0273-1177\(99\)00600-6](https://doi.org/10.1016/S0273-1177(99)00600-6).
- Schrijver, C.J., Harvey, K.L.: 1994, *Solar Phys.* **150**, 1. doi:[10.1007/BF00712873](https://doi.org/10.1007/BF00712873).
- Schrijver, C.J., DeRosa, M.L., Metcalf, T., Barnes, G., Lites, B., Tarbell, T., et al.: 2008, *Astrophys. J.* **675**, 1637. doi:[10.1086/527413](https://doi.org/10.1086/527413).
- Schüssler, M.: 1979, *Astron. Astrophys.* **71**, 79.
- Strous, L.H., Zwaan, C.: 1999, *Astrophys. J.* **527**, 435. doi:[10.1086/308071](https://doi.org/10.1086/308071).
- Titov, V.S., Priest, E.R., Demoulin, P.: 1993, *Astron. Astrophys.* **276**, 564.
- Tsuneta, S., Ichimoto, K., Katsukawa, Y., Nagata, S., Otsubo, M., Shimizu, T., et al.: 2008, *Solar Phys.* **249**, 167. doi:[10.1007/s11207-008-9174-z](https://doi.org/10.1007/s11207-008-9174-z).
- Valori, G., Kliem, B., Keppens, R.: 2005, *Astron. Astrophys.* **433**, 335. doi:[10.1051/0004-6361:20042008](https://doi.org/10.1051/0004-6361:20042008).
- Valori, G., Kliem, B., Fuhrmann, M.: 2007, *Solar Phys.* **245**, 263. doi:[10.1007/s11207-007-9046-y](https://doi.org/10.1007/s11207-007-9046-y).
- Valori, G., Kliem, B., Török, T., Titov, V.S.: 2010, *Astron. Astrophys.* **519**, A44. doi:[10.1051/0004-6361/201014416](https://doi.org/10.1051/0004-6361/201014416).
- Vargas Domínguez, S., van Driel-Gesztelyi, L., Bellot, L.: 2010, *Solar Phys.* submitted.
- Wheatland, M.S., Sturrock, P.A., Roumeliotis, G.: 2000, *Astrophys. J.* **540**, 1150. doi:[10.1086/309355](https://doi.org/10.1086/309355).
- Zwaan, C.: 1985, *Solar Phys.* **100**, 397. doi:[10.1007/BF00158438](https://doi.org/10.1007/BF00158438).